J|A|C|S ARTICLES

Published on Web 12/09/2010

# Surface-Mediated Production of Hydroxyl Radicals as a Mechanism of Iron Oxide Nanoparticle Biotoxicity

Maxim A. Voinov, Jason O. Sosa Pagán, Erin Morrison, Tatyana I. Smirnova, and Alex I. Smirnov*

*Department of Chemistry, North Carolina State University, 2620 Yarbrough Drive, Raleigh, North Carolina 2769-8204, United States*

Received May 29, 2010; E-mail: alex_smirnov@ncsu.edu

***Abstract:*** Emerging applications of nanosized iron oxides in nanotechnology introduce vast quantities of nanomaterials into the human environment, thus raising some concerns. Here we report that the surface of $\gamma$-$Fe_2O_3$ nanoparticles 20−40 nm in diameter mediates production of highly reactive hydroxyl radicals ($OH^{\bullet}$) under conditions of the biologically relevant superoxide-driven Fenton reaction. By conducting comparative spin-trapping EPR experiments, we show that the free radical production is attributed primarily to the catalytic reactions at the nanoparticles' surface rather than being caused by the dissolved metal ions released by the nanoparticles as previously thought. Moreover, the catalytic centers on the nanoparticle surface were found to be at least 50-fold more effective in $OH^{\bullet}$ radical production than the dissolved $Fe^{3+}$ ions. Conventional surface modification methods such as passivating the nanoparticles' surface with up to 935 molecules of oleate or up to 18 molecules of bovine serum albumin per iron oxide core were found to be rather ineffective in suppressing production of the hydroxyl radicals. The experimental protocols developed in this study could be used as one of the approaches for developing analytical assays for assessing the free radical generating activity of a variety of nanomaterials that is potentially related to their biotoxicity.

## Introduction

Rapidly evolving nanotechnology is introducing vast quantities of new engineered nanomaterials (ENMs) into the human environment every day. All of these materials, such as nanoparticles, nanotubes and nanowires, and nanostructured substrates, for example, are expected to interact with biological matrices at some point of their technological cycles, thus raising some unaddressed environmental concerns. One may speculate why nanomaterials would elicit some adverse biological response. (1) The sizes of the dispersed nanomaterials are typically smaller than those of cells, thus allowing for an effective endocytosis and the consequent exposure of ENMs to intracellular components. (2) ENMs are known to exhibit a plethora of entirely new physicochemical properties that cannot be found in the traditional bulk materials. Elements such as gold, for example, although chemically inert at the macroscopic scale, could turn into potent catalysts as nanoparticles.[1] (3) ENMs are characterized by an enormously large surface:volume ratio, thus amplifying many times over the role of chemical processes occurring at the surface that could also be significantly altered compared with the bulk matter. In conclusion, the interfacial and surface properties of ENMs are thought to become the dominant factors in their interactions with biological systems.

Among a wide variety of nanostructures described to date, the nanosized iron oxides are, perhaps, the most widely studied and produced because of numerous promising applications in catalysis, magnetic data storage, multimodal biomedical imaging, targeted drug delivery, and medical diagnostics and therapy.[2−5] While further development of these nanoparticle-based technologies continues, only recently has the issue of biosafety of nanosized iron oxides been given more serious consideration.[6] For instance, a series of cytotoxicity studies revealed some adverse effects of iron oxide nanoparticles composed of either $Fe_3O_4$, $\gamma$-$Fe_2O_3$, or $Fe_2O_3$ both in vivo and in vitro.[7−9] Some of these adverse effects can be effectively mitigated by properly modifying the nanoparticle surface with organic ligands[10] and/or masking the surface under layers of chemically inert elements such as Au.[11] While the exact mechanism of the nanosized iron oxides' biotoxicity is a subject of continuing discussions, results of these biotoxicity studies with surface-modified nanoparticles place the nanoparticles' exceptionally large surface area and an increased number of

(1) Haruta, M.; Daté, M. *Appl. Catal., A* **2001**, *222*, 427–437.
(2) Lu, A.-H.; Salabas, E. L.; Schüth, F. *Angew. Chem., Int. Ed.* **2007**, *46*, 1222–1244.
(3) Fahlvik, A. K.; Klaveness, J. *J. Magn. Reson. Imaging* **1993**, *3*, 187–194.
(4) Sahoo, S. K.; Labhasetwar, V. *Drug Discovery Today* **2003**, *8*, 1112–1120.
(5) Gupta, A. K.; Gupta, M. *Biomaterials* **2005**, *26*, 3995–4021.
(6) Hood, E. *Environ. Health Perspect.* **2004**, *112*, A740–A749.
(7) Auffan, M.; Achouak, W.; Rose, J.; Roncato, M.-A.; Chanéak, C.; Waite, D. T.; Masion, A.; Woicik, J. C.; Wiesner, M. R.; Bottero, J.-Y. *Environ. Sci. Technol.* **2008**, *42*, 6730–6735.
(8) Lewinski, N.; Colvin, V.; Drezek, R. *Small* **2008**, *4*, 26–49.
(9) Wang, B.; Feng, W.; Zhu, M.; Wang, Y.; Wang, M.; Gu, Y.; Ouyang, H.; Wang, H.; Li, M.; Zhao, Y.; Chai, Z.; Wang, H. *J. Nanopart. Res.* **2009**, *11*, 41–53.
(10) Petri-Fink, A.; Chastellain, M.; Juillerat-Jeanneret, L.; Ferrari, A.; Hofmann, A. *Biomaterials* **2005**, *26*, 2685–2694.
(11) Boucharda, L.-S.; Anwarb, M. S.; Liuc, G. L.; Hannc, B.; Xied, Z. H.; Grayc, J. W.; Wange, X.; Pines, A.; Chen, F. F. *Proc. Natl. Acad. Sci. U.S.A.* **2009**, *106*, 4085–4089.

  

surface defects among the most likely causes for the observed toxicological effects.

Another cytotoxicity mechanism currently being discussed in the literature involves reactive oxygen species (ROS) that would evoke an oxidative stress.[8,12] Under a normal cellular biochemical cycle, the ROS are continuously produced and effectively neutralized by available antioxidants such as glutathione and specific enzymes. Evidence that has accumulated in the literature indicates that an increase in the intracellular free iron levels affects the normal ROS−antioxidant balance by promoting ROS production through Fenton and/or Haber−Weiss reactions.[13−15] Several authors speculated that unprotected (bare) iron oxide nanoparticles could release $Fe^{2+}$ ions into an aqueous phase, thus elevating the intracellular iron concentration when the nanoparticles are endocytized and, consequently, causing oxidative damage through the ROS mechanism.[16,17] Experimental studies of intracellular iron concentrations as well as those in cell growth media are supportive of such a hypothesis.[16] However, the surface of iron oxide nanoparticles could also play a role in catalytic ROS production. Indeed, the rate of the reaction between $O_2$ and $Fe^{2+}$ ions absorbed onto a mineral was found to be much faster than in solution.[18] Furthermore, the enormously high surface:volume ratio of ENMs is expected to amplify the role of chemical reactions occurring at the surface.

Here we employ the spin-trapping EPR technique, the most powerful and direct analytical method for quantification of short-lived radicals, to characterize the catalytic ROS production at the surface of iron oxide nanoparticles under conditions of the biologically relevant superoxide-driven Fenton reaction.[19] While many researchers have focused on correlating the nanoparticle optical tracking data in cells and tissues with biological toxicity assays,[20−22] there is an only very limited literature displaying the use of the EPR method for studying ROS production by ENMs according to a recent review.[17] Although optical tracking is an informative approach for following nanoparticles' endocytosis and further intracellular localization, this method sheds no light on the chemistry of the underlying processes. While fluorescent probes that are reactive to ROS have been employed for studying chemical mechanisms,[17] interpretation of the results could be complicated because these probes lack selectivity for specific ROS.[23]

Spin-trapping EPR studies presented here are focused on monitoring the production of hydroxyl radicals ($OH^{\bullet}$) that are thought to be the most harmful among all ROS. Unlike superoxide ($O_2^{\bullet-}$), the hydroxyl radical has a very short intracellular half-lifetime (~1 ns).[24,25] Thus, while the former species are known to persist for a sufficiently long time to be neutralized by the superoxide dismutase enzyme found in oxygen-metabolizing cells, the $OH^{\bullet}$ radicals would react at a rate close to the diffusion-controlled rate with virtually any of the cellular macromolecular components: from oligonucleotides to lipids, proteins, and carbohydrates. Here the production of the $OH^{\bullet}$ radicals has been assessed by trapping these short-lived species by a diamagnetic compound, 5,5-dimethyl-1-pyrroline *N*-oxide (DMPO), and identifying the precursor free radicals from the magnetic parameters of the observed EPR spectra. Two types of commercially available iron oxide nanoparticles, $Fe_3O_4$ and $\gamma$-$Fe_2O_3$ with iron in different oxidation states, $Fe^{II,III}{}_3O_4$ and $Fe^{III}{}_2O_3$, respectively, have been assessed for catalytic ROS production. Comparative spin-trapping EPR experiments performed with nanoparticles passivated with oleate or coated with bovine serum albumin (BSA) as well as control data for $OH^{\bullet}$ production catalyzed by the dissolved $Fe^{3+}$ ions provided further insights into the catalytic activity of the nanoparticle surface centers and the role of the protecting ligands and surface coating.

## Results and Discussion

In biologically relevant systems, hydroxyl radicals are often produced in the course of the Fenton reaction[19] occurring upon decomposition of $H_2O_2$ by a reduced iron complex:

$$Fe^{2+} + H_2O_2 \rightarrow Fe^{3+} + OH^- + OH^{\bullet} \qquad (1)$$

While the short-lived $OH^{\bullet}$ radicals cannot be directly detected by EPR because of the very short lifetime and low steady-state concentrations, they would readily react with diamagnetic nitrone spin trap DMPO, forming a stable free radical (spin adduct) that could be identified from the magnetic parameters of the EPR spectrum.

It should be noted here that the iron oxide nanoparticles are ferromagnetic and, therefore, were found to agglomerate when placed into a magnetic field of an EPR spectrometer causing undesirable nonresonant losses of microwave energy. In addition, these nanoparticles give rise to a strong ferromagnetic resonance signal that overlaps with much weaker lines from spin adducts. Thus, to avoid these problems, we conducted the EPR experiments as follows. First, the nanoparticles were incubated with a $H_2O_2$ and DMPO solution and then separated by centrifugation from a clear supernatant. The latter was transferred into a polytetrafluoroethylene (PTFE) capillary for EPR measurements. In absence of catalytic centers such as, for example, dissolved transition metal ions or catalytic sites at the surface of the nanoparticles, the amplitude of EPR signals from DMPO spin adducts is low (Figure 1A) when compared to the noise level. A similar very weak EPR signal was observed upon incubation of the same $H_2O_2$ and DMPO solution with $\gamma$-$Fe_2O_3$ nanoparticles (Figure 1B). Nevertheless, four weak lines with approximately equal spacing of ca. 14.9 G that is consistent with the hyperfine splitting reported for the DMPO−$OH^{\bullet}$ spin adduct[26] can be identified in Figure 1B. Incubation of $H_2O_2$ and DMPO with a $FeCl_3$ solution containing iron in the same oxidation state as $\gamma$-$Fe_2O_3$ nanoparticles results in a significantly stronger four-line EPR signal with a 1:2:2:1 peak-to-peak intensity pattern (Figure 1C) and the isotropic hyperfine coupling

(12) Nel, A.; Xia, T.; Mädler, L.; Li, N. *Science* **2006**, *311*, 622–627.
(13) Gutteridge, J. M.; Rowley, D. A.; Halliwell, B. *Biochem. J.* **1982**, *206*, 605–609.
(14) Emerit, J.; Beaumont, C.; Trivin, F. *Biomed. Pharmacother.* **2001**, *55*, 333–339.
(15) Hills, C. J.; Winter, S. A.; Balfour, J. A. *Drugs* **1998**, *55*, 813–820.
(16) Arbab, A. S.; Bashaw, L. A.; Miller, B. R.; Jordan, E. K.; Lewis, B. K.; Kalish, H.; Frank, J. A. *Radiology* **2003**, *229*, 838–846.
(17) Marquis, B. J.; Love, S. A.; Braun, K. L.; Haynes, C. L. *Analyst* **2009**, *134*, 425–439.
(18) Wehrli, B.; Sulzberger, B.; Stumm, W. *Chem. Geol.* **1989**, *78*, 167–179.
(19) Fenton, H. J. H. *J. Chem. Soc.* **1894**, *65*, 899–910.
(20) Bergey, E. J.; Levy, L.; Wang, X.; Krebs, L. J.; Lal, M.; Kim, K.-S.; Pakatchi, S.; Liebow, C.; Prasad, P. N. *Biomed. Microdevices* **2002**, *4*, 293–299.
(21) Yu, K. O.; Grabinski, C. M.; Schrand, A. M.; Murdock, R. C.; Wang, W.; Gu, B.; Schlager, J. J.; Hussain, S. M. *J. Nanopart. Res.* **2009**, *11*, 15–24.
(22) Yum, K.; Na, S.; Xiang, Y.; Wang, N.; Yu, M.-F. *Nano Lett.* **2009**, *9*, 2193–2198.
(23) Soh, N. *Anal. Bional. Chem.* **2006**, *386*, 532–543.
(24) Beauchamp, C.; Fridovich, I. *J. Biol. Chem.* **1970**, *245*, 4641–4646.
(25) Halliwell, B.; Gutteridge, J. M. C. *FEBS Lett.* **1992**, *307*, 108–112.
(26) Minotti, G.; Aust, S. D. *J. Biol. Chem.* **1987**, *262*, 1098–1104.


***Figure 1.*** X-Band (9.5 GHz) EPR spectra of phosphate-buffered (50 mM, pH 7.4) aqueous solutions of (A) $H_2O_2$ (0.45 mM) and DMPO (34.25 mM) after incubation for 20 min, (B) 80 $\mu$L of the same solution used for spectrum A incubated with $\gamma$-$Fe_2O_3$ nanoparticles (3.04 mg, $\approx 2.01 \times 10^{13}$ particles, total nanoparticle surface area of 0.0912 $m^2$), (C) $H_2O_2$ (0.36 mM), DMPO (27.6 mM), and $FeCl_3$ (0.24 mM), (D) the same solution that was used for spectrum B but with $Fe_3O_4$ nanoparticles (3.04 mg, $\approx 4.48 \times 10^{13}$ particles, total nanoparticle surface area of 0.1216 $m^2$), and (E) 50 $\mu$L of the buffer incubated for 1 h with 3.4 mg of $Fe_3O_4$ nanoparticles (the nanoparticles were separated by centrifugation, and DMPO and $H_2O_2$ were added at the final concentrations described for spectrum D). All spectra are averages of 100 scans measured at identical spectrometer settings. All incubations and spectra averaging were conducted at 37 °C. See Materials and Methods for further details.

constants ($A_N = A_H \approx 14.9$ G) that are characteristic of the DMPO−$OH^{\bullet}$ adduct.[26] The most likely reason for formation of $OH^{\bullet}$ radicals in the latter two systems is that the $Fe^{3+}$ ions decompose $H_2O_2$ slowly, compared to $Fe^{2+}$, in accord with the previously introduced reaction scheme:[27]

$$Fe^{3+} + H_2O_2 \rightarrow FeOOH^{2+} + H^+ \quad (2)$$

$$FeOOH^{2+} \rightarrow Fe^{2+} + HO_2^{\bullet} \quad (3)$$

$$Fe^{2+} + H_2O_2 \rightarrow Fe^{3+} + OH^- + OH^{\bullet} \quad (4)$$

The same spin-trapping experiments were repeated with $Fe_3O_4$ nanoparticles that contain both $Fe^{2+}$ and $Fe^{3+}$ ions at the surface in an approximately 1:2.6 ratio, which was confirmed by X-ray photoelectron spectroscopy (XPS). Further details of the XPS analysis of the $Fe_3O_4$ nanoparticles are provided on page S8 of the Supporting Information. For these nanoparticles, the magnitude of the DMPO−$OH^{\bullet}$ adduct EPR signal increased between 4- and 5-fold (Figure 1D) in comparison to that of the $\gamma$-$Fe_2O_3$ nanoparticle experiment (Figure 1B). Note that the specific surface area of the $Fe_3O_4$ nanoparticles ($\approx$40 $m^2$/g) is only modestly greater than that of the $\gamma$-$Fe_2O_3$ nanoparticles ($\approx$30 $m^2$/g). This modest difference would not account for the relative magnitudes of the DMPO−$OH^{\bullet}$ adduct EPR signals observed in our experiments (Figure 1). Thus, as one would expect from considerations of the iron oxidation state, the $Fe_3O_4$ nanoparticles are significantly more effective in producing $OH^{\bullet}$ radicals than the $\gamma$-$Fe_2O_3$ nanoparticles at the same ratio of the nanoparticle total surface and reaction volume.

One possible mechanism of nanoparticle toxicity discussed in the literature involves generation of $OH^{\bullet}$ radicals by iron ions leaching from the nanoparticles into a solution.[16,17] The efficiency of this mechanism was evaluated in the following experiment. First, the $Fe_3O_4$ nanoparticles were incubated in a 50 mM phosphate buffer solution (pH 7.4) for 1 h at 37 °C. The nanoparticles were separated from the solution by centrifugation, and only then were the spin trap DMPO and $H_2O_2$ added to the clear supernatant. While the presence of the DMPO−$OH^{\bullet}$ spin adduct in this supernatant sample still can be identified from the EPR spectrum (Figure 1E), its intensity is significantly lower than in the experiment with the $Fe_3O_4$ nanoparticles (Figure 1D). The results of this experiment clearly demonstrate that the observed $OH^{\bullet}$ radical production primarily occurs at the nanoparticle surface rather than being catalyzed by the iron ions leached into the solution as previously thought.

Another efficient pathway for producing $OH^{\bullet}$ in biological systems is known to be provided by a superoxide-driven Fenton reaction, also known as Haber−Weiss reactions:[28,29]

$$Fe^{3+} + O_2^{\bullet -} \rightarrow Fe^{2+} + O_2 \quad (5)$$

$$2O_2^{\bullet -} + 2H^+ \rightarrow H_2O_2 + O_2 \quad (6)$$

$$Fe^{2+} + H_2O_2 \rightarrow Fe^{3+} + OH^- + OH^{\bullet} \quad (7)$$

In this catalytic cycle, the superoxide, $O_2^{\bullet -}$, acts as both a reductant for $Fe^{3+}$ and a precursor for $H_2O_2$; the final step (eq 7) is the conventional Fenton reaction. In living systems, the superoxide radical and hydrogen peroxide are produced in both intra- and extracellular volumes by activated phagocytes,[30] lymphocytes,[31] endothelial cells,[32] and fibroblasts[33] and also through a "leakage" of electrons from the electron transport chain.[34]

To investigate whether the $\gamma$-$Fe_2O_3$ nanoparticles would participate in the Haber−Weiss cycle in a manner similar to that of the dissolved $Fe^{3+}$ ions, we added a xanthine/xanthine oxidase (X/XO) superoxide generating system to the reaction mixture.[35] It should be noted that the DMPO−$OH^{\bullet}$ spin adduct could be formed not only through the authentic $OH^{\bullet}$ radical scavenging mechanism but also in the course of a decay of the DMPO−superoxide adduct.[36,37] To prevent formation of the DMPO−superoxide adduct and to exclude its decomposition as a pathway for formation of the DMPO−$OH^{\bullet}$ adduct, we conducted the experiments as follows. An aqueous solution of $Fe(NO_3)_3$ or a suspension of $\gamma$-$Fe_2O_3$ nanoparticles was initially

(27) Perez-Benito, J. F. *J. Phys. Chem. A* **2004**, *108*, 4853–4858.
(28) McCord, J. M.; Day, E. D. *FEBS Lett.* **1978**, *86*, 139–142.
(29) Halliwell, B.; Gutteridge, J. M. C. *Methods Enzymol.* **1990**, *186*, 1–85.
(30) Babior, B. M.; Woodman, R. C. *Semin. Hematol.* **1990**, *27*, 247–259.
(31) Maly, F. E. *Free Radical Res. Commun.* **1990**, *8*, 143–148.
(32) Babbs, C. F.; Cregor, M. D.; Turek, J. J.; Badylak, S. F. *Lab. Invest.* **1991**, *65*, 484–496.
(33) Murrell, G. A. C.; Francis, M. J. O.; Bromley, L. *Biochem. J.* **1990**, *265*, 659–665.
(34) Fridovich, I. *J. Biol. Chem.* **1989**, *264*, 7761–7764.
(35) Beauchamp, C.; Fridovich, I. *Anal. Biochem.* **1970**, *44*, 276–287.
(36) Finkelstein, E.; Rosen, G. M.; Rauckman, E. J. *Arch. Biochem. Biophys.* **1980**, *200*, 1–16.
(37) Finkelstein, E.; Rosen, G. M.; Rauckman, E. J. *Mol. Pharmacol.* **1982**, *21*, 262–265.

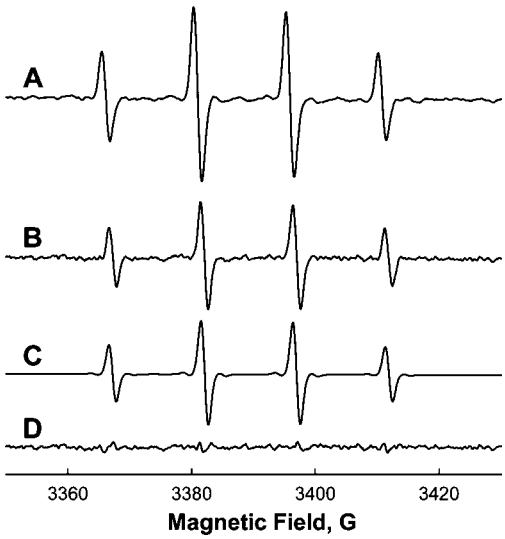


***Figure 2.*** X-Band (9.5 GHz) EPR spectra (37 °C) of the DMPO−OH• adduct obtained under the following conditions: (A) an incubation of 0.089 mM $Fe(NO_3)_3$, 15.54 mM EDTA, 5.18 mM xanthine, 1.1 milliunits/mL xanthine oxidase with a consequent addition of 0.13 mM $H_2O_2$, and 10.22 mM DMPO and (B) an incubation of 3.04 mg of $\gamma$-$Fe_2O_3$ nanoparticles, 7 mM xanthine, 3 milliunits/mL xanthine oxidase, and 21 mM EDTA followed by separation of nanoparticles and incubation of them with 80 $\mu$L of a solution of 0.45 mM $H_2O_2$ and 34.5 mM DMPO. Spectrum C is a least-squares simulation of spectrum B with the following best-fit hyperfine parameters: $A_N = 14.91 \pm 0.01$ G, and $A_H = 14.90 \pm 0.01$ G. Spectrum D is the fit residual minus the difference between the experimental and simulated spectrum. All spectra were recorded at identical spectrometer settings; however, the vertical scale of this figure was decreased 3-fold vs that of Figure 1. See the text for further details.

incubated with the X/XO superoxide generating system at 37 °C for 20 min (this reaction was monitored by UV−vis spectroscopy at 295 nm, and 20 min was found to be sufficient for xanthine to be consumed by xanthine oxidase). Consequently, a clear supernatant was separated by centrifugation and discarded. The precipitated nanoparticles were incubated with $H_2O_2$ and DMPO with occasional vortexing for an additional 40 min before the EPR spectra were recorded at the same temperature (Figure 2).

Figure 2A shows the results of a control experiment for generating hydroxyl radicals in the course of the conventional Haber−Weiss reaction cycle initiated by the dissolved $Fe^{3+}$ ions. The EPR spectrum from the final supernatant reveals a clear four-line hyperfine pattern with 1:2:2:1 intensity ratios that is characteristic for the DMPO−OH• adduct. Least-squares simulations (not shown) yielded the following isotropic hyperfine coupling constants that are in a good agreement with literature data:[26] $A_N = 14.91 \pm 0.01$ G, and $A_H = 14.90 \pm 0.01$ G.

Figure 2B shows an EPR spectrum acquired from a supernatant of the reaction mixture containing $\gamma$-$Fe_2O_3$ nanoparticles. When compared with the spectrum obtained in the absence of X/XO (Figure 1B), a drastic increase in the amplitude of the DMPO−OH• adduct EPR signal becomes evident (note that the vertical scale of Figure 2 is decreased 3-fold to accommodate the stronger signals). This gain in the level of OH• radical generation indicates that the major effect of the superoxide anion on the $\gamma$-$Fe_2O_3$ nanoparticle surface chemistry is in changing the redox state of the catalytic centers as shown in eq 5. The fact that the spectrum in Figure 2B reveals no fine structure characteristic of the $O_2^{\bullet-}$ adduct[38−40] verifies that essentially all the superoxide produced by the X/XO system has been consumed (oxidized by $Fe^{3+}$) prior to the DMPO spin-trapping step.

Another important observation is that in the X/XO−$H_2O_2$/DMPO experiment the EPR intensity of the DMPO−OH• signal obtained upon incubation with $\gamma$-$Fe_2O_3$ nanoparticles is ~62% of that found when a 89 $\mu$M solution of $Fe(NO_3)_3$ was used to catalyze the radical production instead of the nanoparticles (compare spectra B and A of Figure 2). Assuming that every $Fe^{3+}$ ion on the nanoparticle surface is participating in the Haber−Weiss reactions with a steric coefficient of 0.5 (to account for a limited accessibility of the surface sites) and that the $\gamma$-$Fe_2O_3$ crystal cell parameters[41,42] are also valid for the nanoparticle surface, one estimates that the concentration of the nanoparticle surface catalytic sites should be equivalent to less than 1 $\mu$M of the bulk concentration of the dissolved centers. By comparing this value with the $Fe(NO_3)_3$ concentration of 89 $\mu$M that was used in the control experiment in addition to correcting for the ratio of the EPR double-integrated intensities, one concludes that the catalytic centers on the $\gamma$-$Fe_2O_3$ surface are at least 50-fold more effective as hydroxyl radical promoters than the dissolved ions. Thus, not only the vast surface:volume ratio of the $\gamma$-$Fe_2O_3$ nanoparticles but also the greatly enhanced catalytic activity of the surface centers is responsible for the effective production of hydroxyl radicals in the course of the Haber−Weiss cycle.

To further confirm that the main pathway for the formation of the DMPO−OH• adduct in our experiments is indeed the reaction of DMPO with OH•, we added 20 molar equiv (vs DMPO) of a highly specific hydroxyl radical scavenger dimethyl sulfoxide (DMSO)[43−45] to either $Fe_3O_4$ or $\gamma$-$Fe_2O_3$ nanoparticles prior to the addition of DMPO and $H_2O_2$. In both experiments, formation of the DMPO−OH• adduct was almost completely inhibited (Figure S5 of the Supporting Information). Via comparison of the double integral intensity ratio of the original (Figure 2B) EPR spectra versus those obtained in the course of the DMSO inhibition experiments with superoxide-activated $\gamma$-$Fe_2O_3$ nanoparticles (≈0.984:0.105 as determined by least-squares simulations), it was estimated that at least 89 ± 2% of the DMPO−OH• adducts detected in the original experiment was formed via the OH• radical trapping mechanism. When the same DMSO inhibition experiment was conducted with $Fe_3O_4$ nanoparticles, the intensity of the DMPO−OH• adduct EPR signal was at the noise level (Figure S6 of the Supporting Information), allowing us to estimate that >90% of the DMPO−OH• adducts measured in the original experiment (Figure 1D) were formed through the OH• radical scavenging mechanism.

(38) Harbour, J. R.; Chow, V.; Bolton, J. R. *Can. J. Chem.* **1974**, *52*, 3549–3553.
(39) Vásquez-Vivar, J.; Kalyanaraman, B. *FEBS Lett.* **2000**, *481*, 305–306.
(40) Dikalov, S.; Jiang, J.; Mason, R. P. *Free Radical Res.* **2005**, *39*, 825–836.
(41) Pecharromán, C.; González-Carreño, T.; Iglesias, J. E. *Phys. Chem. Miner.* **1995**, *22*, 21–29.
(42) Cudennec, Y.; Lecerf, A. *Solid State Sci.* **2005**, *7*, 520–529.
(43) Dorfman, L. M.; Adams, G. E. *Natl. Stand. Ref. Data Ser. (U.S., Natl. Bur. Stand.)* **1973**, *46*, 1–59.
(44) Rosenblum, W. I.; El-Sabban, F. *Stroke* **1982**, *13*, 35–39.
(45) Steiner, M. G.; Babbs, C. F. *Arch. Biochem. Biophys.* **1990**, *278*, 478–481.

**Hydroxyl Radical Production by Oleate- and BSA-Coated Iron Oxide Nanoparticles.** While the link between bare (unprotected) iron oxide nanoparticles and some cytotoxic effects has been well established,[7−9] modification of the nanoparticle surface with certain ligands[10] or coating those with bovine serum albumin (BSA)[46] is known to alleviate the cytoxicity problem in a dose-dependent manner.[10,46] Thus, one may hypothesize that these surface modifications would have some inhibiting effects on the surface-mediated production of reactive free radicals.

To test this hypothesis, oleate- and BSA-coated $\gamma$-$Fe_2O_3$ nanoparticles were prepared according to the literature procedures.[47,48] The FT-IR spectrum of the oleate-passivated $\gamma$-$Fe_2O_3$ nanoparticles (Figure S1 of the Supporting Information) was found to be identical to that reported in the literature.[48] The FT-IR spectrum of the BSA-coated $\gamma$-$Fe_2O_3$ nanoparticles revealed vibrational bands at 1643 and 1521 $cm^{-1}$ (Figure S2 of the Supporting Information), in close agreement with literature data.[47] The amount of organic material absorbed on the nanoparticle surface was determined by thermogravimetric analysis (TGA) (see Figures S3 and S4 of the Supporting Information). The 2.1% weight loss determined via TGA of the oleate-coated particles corresponds to ∼935 oleate molecules per nanoparticle. At such a low oleate:nanoparticle ratio, only an oleate monolayer was supposed to be formed.[49] To further estimate the area of the nanoparticle surface coated with oleic acid, the latter was considered as a molecule with a cylindrical topology. Given a molecular volume of oleic acid of 0.475 $nm^3$ (ref 50) and a chain length of 2.8 ± 0.1 nm,[51] the surface area occupied by one oleic acid molecule is ∼0.17 $nm^2$. Then if one assumes that ∼935 oleic acid molecules form a monolayer on a surface of a spherical nanoparticle 30 nm in diameter, only ∼56% of the nanoparticle surface will be covered. Such a loose imperfect coating is expected to leave the nanoparticle surface accessible to small solute molecules.

The 8.35−9.65% weight loss observed via TGA of BSA-coated particles corresponds to ∼16−18 BSA molecules per nanoparticle. The range of BSA coating arises from TGA analysis of three batches of coated nanoparticles prepared on different days. If one assumes a side-on orientation of BSA on a surface and BSA molecular dimensions of ≈11.6 nm × ≈2.7 nm × ≈2.7 nm,[52] then the fraction of the nanoparticle surface coated by BSA is only ∼12%. This value is somewhat lower than the one reported in the literature (ca. 22%)[47] and is likely related to some differences between the surface properties of the previously reported freshly prepared nanoparticles[47] and those of the commercial ones studied here. Of course, one may not exclude a denaturing of some BSA on the nanoparticle surface that may increase the surface coverage.

The coated $\gamma$-$Fe_2O_3$ nanoparticles were then employed in spin-trapping EPR experiments to investigate their participation in either the Fenton reaction or the Haber−Weiss cycle using the same protocols. While under conditions of the Fenton reaction the EPR signal (Figure 3A) was similarly weak when compared with that of the unprotected nanoparticles (Figure 1B), the final supernatant solution obtained from the oleate-coated $\gamma$-$Fe_2O_3$ nanoparticles and X/XO−$H_2O_2$/DMPO system revealed a distinct 1:2:2:1 four-line pattern with the following isotropic hyperfine coupling constants that are typical for the DMPO−$OH^•$ spin adducts:[26] $A_N = 14.91 \pm 0.01$ G, and $A_H = 14.90 \pm 0.01$ G (Figure 3B). Thus, the loose oleate layer formed by ∼935 molecules per nanoparticle appears to present little, if any, hindrance for small molecules such as $O_2^{•-}$, $H_2O_2$, and DMPO to freely diffuse to and from the nanoparticle surface. Moreover, these results indicate that as in the reaction with uncoated $\gamma$-$Fe_2O_3$ nanoparticles, $O_2^{•-}$ appears to be effective in reducing the oleate-passivated $Fe_2O_3$ surface, which in turn would promote decomposition of $H_2O_2$ and formation of the $OH^•$ radical.

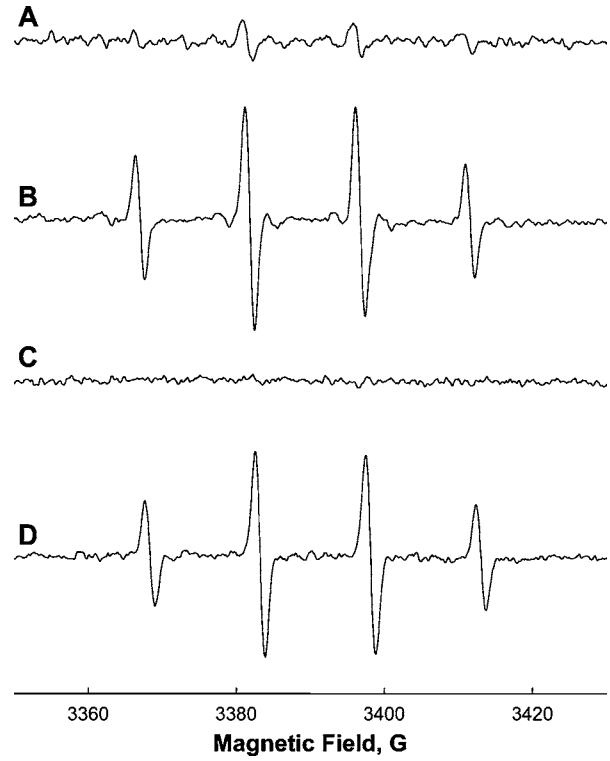


***Figure 3.*** X-Band (9.5 GHz) EPR spectra (37 °C) of the DMPO−$OH^•$ adduct obtained from (A) oleate-passivated $\gamma$-$Fe_2O_3$ nanoparticles under conditions of the Fenton reaction protocol (0.45 mM $H_2O_2$ and 34.25 mM DMPO) and (B) the Haber−Weiss cycle protocol (7 mM xanthine, 3 milliunits/mL xanthine oxidase, 21 mM EDTA, supernatant discarded after centrifugation, and 0.45 mM $H_2O_2$ and 34.5 mM DMPO added to $\gamma$-$Fe_2O_3$ nanoparticles), (C) BSA-coated $\gamma$-$Fe_2O_3$ nanoparticles under conditions of the same Fenton reaction, and (D) the Haber-Weiss cycle. In all experiments, the same number of $\gamma$-$Fe_2O_3$ nanoparticles (≈$2.01 \times 10^{13}$) was incubated with the same 80 $\mu$L of the reaction mixture. The signals were renormalized to identical spectrometer settings.

When the same sequence of experiments was repeated for BSA-coated $\gamma$-$Fe_2O_3$ nanoparticles, the results were found to be nearly identical: the Fenton reaction protocol yielded no detectable EPR signal (Figure 3C), while the same Haber−Weiss protocol resulted in the characteristic EPR spectrum of the DMPO−$OH^•$ adduct with a similar intensity (Figure 3D). Overall, six spin-trapping experiments with BSA-coated nanoparticles from three batches prepared at different time have been conducted, yielding nearly identical results with the exception of one experiment in which no measurable DMPO−$OH^•$ adduct

(46) Gupta, A. K.; Gupta, M. *Biomaterials* **2005**, *26*, 1565–1573.
(47) Samanta, B.; Yan, H.; Fischer, N. O.; Shi, J.; Jerry, D. J.; Rotello, V. M. *J. Mater. Chem.* **2008**, *18*, 1204–1208.
(48) Gupta, A. K.; Curtis, A. S. G. *Biomaterials* **2004**, *25*, 3029–3040.
(49) Hajdú, A.; Tombácz, E.; Illés, E.; Bica, D.; Vékás, L. *Prog. Colloid Polym. Sci.* **2008**, *135*, 29–37.
(50) Requena, J.; Haydon, D. A. *Proc. R. Soc. London, Ser. A* **1975**, *347*, 161–177.
(51) White, S. H.; King, G. I. *Proc. Natl. Acad. Sci. U.S.A.* **1985**, *82*, 6532–6536.
(52) Yoon, J.-Y.; Garrell, R. L.; Choi, S.-W.; Kim, J.-H.; Kim, W.-S. *AIChE J.* **2005**, *51* (3), 1048–1052.

EPR signal was detected. The latter was attributed to a failure of the X/XO system to generate superoxide, and the results of this experiment were discarded.

The absence of any significant effects of both types of nanoparticle coating on the hydroxyl radical production is likely attributed to a rather loose structure of the protective layer and/or incomplete surface coverage. Indeed, from simple geometrical considerations presented above, the entire nanoparticle surface cannot be blocked with just 16−18 BSA molecules. Our observation appears to be in disagreement with a recent report that the BSA-passivated $Fe_3O_4$ nanoparticles do not display any measurable cytotoxicity with respect to cancerous HeLa cells.[47] However, the fact that the viability of the HeLa cells was not diminished by the BSA-coated nanoparticles does not guarantee the absence of effects on other cell types. It is well documented that internalization of proteins requires specific membrane receptors, and therefore, different cell types take up BSA with different efficacies (see, for example, refs 53 and 54). Furthermore, the HeLa cells are known to show a weak tendency to internalize objects coated with BSA, which has been demonstrated for BSA-coated latex beads.[55] Other researchers found no evidence that latex beads protected with bovine serum albumin were internalized into HeLa cells.[56] Thus, the absence of cytotoxicity reported in ref 47 might be attributed to a failure of the BSA-passivated $Fe_3O_4$ nanoparticles to be internalized by these cells rather than a change in surface catalytic properties.

For BSA-coated nanoparticles, the catalytic production of hydroxyl radicals occurring in the immediate proximity of the BSA surface residues would result in generation of secondary species such as carbon- and sulfur-centered radicals. One may expect such radicals to be trapped by DMPO and detected by EPR from the distinctive spectral features. In our experiment, the nanoparticles were separated from the supernatant before the EPR measurements. Unfortunately, exceptionally strong ferromagnetic resonance from the $\gamma$-$Fe_2O_3$ nanoparticle core in the $g = 2$ region prevented us from detecting such spin adducts by EPR from the precipitate collected after the DMPO/$H_2O_2$ incubation stage. The experimental spectrum of the supernatant shown in Figure 3D does not reveal any other signals except that of the DMPO−OH$^\bullet$ adduct. Thus, we conclude that even if BSA may react with hydroxyl radicals generated at the nanoparticle surface and these secondary species could react with DMPO, the release of these additional DMPO adducts into solution is insignificant for EPR detection. Additional TGA data from the collected precipitate showed essentially the same weight loss, confirming that none of the coating has been lost after all these procedures.

It is worth noting here that complete blockage of the iron oxide nanoparticle surface with organic and/or bioorganic ligands represents an experimentally difficult task. Thus, other approaches should be pursued for alleviating the cytotoxicity of the nanoparticles with imperfect surface coverage. For example, pullulan-coated iron oxide nanoparticles were found not to be cytotoxic even if they are effectively internalized by human fibroblast cells.[46] We speculate that the low cytotoxicity of such particles could be attributed to the free radical scavenging activity that was reported recently for polysaccharides.[57−60] Further experiments will be required to clarify this issue as no further data on the coating of iron oxide nanoparticles employed in human fibroblast studies, such as average number of the pullulan ligands per nanoparticle, have been reported.[4]

## Conclusions

In conclusion, by conducting a series of spin-trapping EPR experiments, we showed for the first time that the surface of unprotected $\gamma$-$Fe_2O_3$ nanoparticles mediates production of highly reactive hydroxyl radicals (OH$^\bullet$) under conditions of the biologically relevant superoxide-driven Fenton reaction, also known as the Haber−Weiss cycle. The test conducted with iron ions leached from the nanoparticles confirmed that the observed catalytic activity of the $\gamma$-$Fe_2O_3$ and $Fe_3O_4$ nanoparticles is attributed primarily to the reactions at the nanoparticles' surface, rather than being caused by the dissolved metal ions released by the nanoparticles as previously thought. Furthermore, the catalytic centers on the nanoparticle surface were found to be at least 50-fold more effective in the production of the OH$^\bullet$ radical than the dissolved $Fe^{2+}$ ions. Thus, not only the vast surface:volume ratio of the iron oxide nanoparticles but also the greatly enhanced catalytic activity of the surface centers is responsible for the effective production of hydroxyl radicals in the course of the Haber−Weiss cycle. Passivating the nanoparticles' surface with up to 935 molecules of oleate or up to 18 molecules of bovine serum albumin per iron oxide core has little effect on the catalytic production of the hydroxyl radicals. Taking these results together indicates that the cytotoxic effects of iron oxide nanoparticles may not be effectively alleviated by the loose steric protection of the nanoparticle iron oxide core that is achieved using conventional surface modification methods. From a practical perspective, the tight and uniform coating of the nanoparticle core that would prevent diffusion of small molecules may be difficult to achieve, and therefore, other strategies such as coatings with radical-scavenging ligands may be more effective. The latter strategies may be further tested using the experimental protocols developed in this study. Thus, conventional surface modification methods were found to be rather ineffective in suppressing the catalytic production of hydroxyl radicals at the surface of the iron oxide nanoparticles. Overall, spin-trapping EPR experimental protocols developed in this study could be used as one of the approaches for developing analytical assays for assessing the free radical generating activity of a variety of nanomaterials that is potentially related to their biotoxicity.

## Materials and Methods

**Nanoparticles and Chemicals.** $Fe_3O_4$ (20−30 nm) and $\gamma$-$Fe_2O_3$ (20−40 nm) nanoparticles with a spherical morphology were purchased from NanoAmor Inc. (Houston, TX; stock nos. 2650TR and 2540XW, respectively) and used as received. Parameters of the nanoparticles are summarized in Table 1. To elucidate the $Fe^{2+}$:$Fe^{3+}$ atomic ratio at the surface of $Fe_3O_4$ nanoparticles, we measured the high-resolution XPS spectra (see the Supporting Information).

(53) Lotti, L. V.; Hand, A. R. *Cell Tissue Res.* **1989**, *255* (2), 333–342.
(54) Gire, V.; Kostrouch, Z.; Bernier-Valentin, F.; Rabilloud, R.; Munari-Silem, Y.; Rousset, B. *Endocrinology* **1996**, *137*, 522–532.
(55) Garduño, R. A.; Garduño, E.; Hoffman, P. S. *Infect. Immun.* **1998**, *66* (10), 4602–4610.
(56) Goluszko, P.; Selvarangan, R.; Popov, V.; Pham, T.; Wen, J. W.; Singhal, J. *Infect. Immun.* **1999**, *67* (8), 3989–3997.
(57) Zhang, Q.; Li, N.; Zhou, G.; Lu, X.; Xu, Z.; Li, Z. *Pharmacol. Res.* **2003**, *48*, 151–155.
(58) Kayali, H.; Ozdag, M. F.; Kahraman, S.; Aydin, A.; Gonul, E.; Sayal, A.; Odabasi, Z.; Timurkaynak, E. *Neurosurg. Rev.* **2005**, *28*, 298–302.
(59) Wang, J.; Zhang, Q.; Zhang, Z.; Li, Z. *Int. J. Biol. Macromol.* **2008**, *42*, 127–132.
(60) Pasanphan, W.; Buettner, G. R.; Chirachanchai, S. *Carbohydr. Res.* **2010**, *345*, 132–140.

***Table 1.*** Iron Oxide Nanoparticle Parameters[a]

| | $\gamma$-$Fe_2O_3$ | $Fe_3O_4$ |
|---|---|---|
| purity (%) | 96 | 98 |
| average diameter (nm) | 20−40 | 20−30 |
| specific surface area ($m^2$/g) | 30 | 40 |

[a] All nanoparticles have a spherical morphology. All parameters were specified by NanoAmor Inc.

XPS analysis was performed with Kratos Analytical Axis Ultra (Kratos Analytical, Manchester, U.K.) installed at the Shared Materials Instrumentation Facility (SMIF) of Duke University (Durham, NC). DMPO (5,5-dimethyl-1-pyrroline *N*-oxide), bovine serum albumin (BSA), and xanthine were purchased from Sigma-Aldrich (Milwaukee, WI). Xanthine oxidase (XO) with a specific activity of approximately 1 unit/mL was purchased from Roche Diagnostics Corp. (Indianapolis, IN). Other chemicals were purchased from VWR International (West Chester, PA) if not stated otherwise.

Oleate- and BSA-coated $\gamma$-$Fe_2O_3$ nanoparticles were synthesized in a manner similar to the literature procedures.[47,48] FT-IR spectra were recorded with a Jasco (Easton, MD) FT-IR 410 spectrometer. Thermogravimetric analysis was conducted with a TA Instruments (New Castle, DE) TGA Q50 V6.7 Build 203 thermogravimetric analyzer. For FT-IR spectra and data of TGA, see the Supporting Information.

The following stock solutions were prepared and used in the work: 137 mM DMPO in a 50 mM phosphate buffer solution (pH 7.0), 0.6 mM $H_2O_2$ in a 50 mM phosphate buffer solution (pH 7.0), 1.2 mM $FeSO_4$, $FeCl_3$, or $Fe(NO_3)_3$ in deionized water, a 10 mM xanthine solution in 50 mM phosphate buffer containing 30 mM EDTA (pH 8.0), and 0.01 unit/mL xanthine oxidase in a 50 mM phosphate buffer solution (pH 7.38). Only freshly prepared xanthine, xanthine oxidase, and $H_2O_2$ solutions were used in the experiments; other stock solutions were purged with argon and kept at 4 °C between experiments.

*EPR measurements* were taken at 37 °C with a Varian (Palo Alto, CA) Century Series E-109 spectrometer. The temperature was maintained with stability better than ±0.02 °C and a gradient below 0.07 °C/cm over the sample region by a digital variable temperature accessory described previously.[61] In a typical experiment, an aqueous solution was drawn into polytetrafluoroethylene (PTFE) capillary (0.81 mm × 1.12 mm, NewAge Industries, Inc., Southampton, PA), and the capillary was folded twice and inserted into a standard 3 mm × 4 mm quartz EPR tube (Wilmad-LabGlass, Vineland, NJ). The data acquisition parameters were set as follows: modulation amplitude, 0.8 G; microwave power, 2 mW; scan width, 100 G; sweep time, 30 s; time constant, 32 ms. Typically, 100 scans were collected and averaged. Fast-motion EPR spectra of the spin adducts were least-squares simulated using a fast-exchange model with software described previously.[62,63] The pH of all the EPR samples was in the range of 7.6−7.8.

**EPR Spin-Trapping Experiments. (1) Solution Experiments.** A solution containing $H_2O_2$ (0.36 mM) and DMPO (27.6 mM) was incubated with $FeCl_3$ or $Fe(NO_3)_3$ (0.24 mM) at 37 °C for 20 min and transferred to a PTFE capillary for EPR measurements.

**(2) Solution Experiments with the Xanthine/Xanthine Oxidase System.** A solution containing $FeCl_3$ or $Fe(NO_3)_3$ (0.089 mM), XO (1.1 milliunits/mL), xanthine (5.18 mM), and EDTA (15.54 mM) was incubated at room temperature for 20 min, and then $H_2O_2$ (60 $\mu$L, 0.036 $\mu$M) and DMPO (20 $\mu$L, 2.74 $\mu$M) were added; the resulting solution was occasionally vortexed for 1.5−2 min and quickly transferred into a PTFE capillary for EPR measurements. The optimal incubation time (20 min) was determined as follows. A solution containing xanthine (5 mM), xanthine oxidase (0.21 milliunits/mL), and EDTA (15 mM) was placed in the UV cell, and the conversion of xanthine to urate was monitored with a UV−vis Hewlett-Packard (Santa Clara, CA) 8453 spectrophotometer at 295 nm.[64] In this experiment, EDTA was added to prevent a known inhibition of xanthine oxidase by the trace metals.[64]

**(3) Experiments with Nanoparticles.** Eighty microliters of a solution containing $H_2O_2$ (0.45 mM) and DMPO (34.5 mM) was incubated with $\gamma$-$Fe_2O_3$ (3.04 mg, ≈$2.01 \times 10^{13}$ particles, total nanoparticle surface area of 0.0912 $m^2$) or $Fe_3O_4$ (3.04 mg, ≈$4.48 \times 10^{13}$ particles, total nanoparticle surface area of 0.1216 $m^2$) nanoparticles at 37 °C for 20 min with occasional vortexing. The resulting mixture was spun down by centrifugation at 11000 rpm for 5 min, and a clear supernatant solution was transferred to a PTFE capillary for EPR measurements.

**(4) Experiments with Nanoparticles and the Xanthine/Xanthine Oxidase System.** $\gamma$-$Fe_2O_3$ nanoparticles (3.04 mg) were placed into a conical vial, and then 140 $\mu$L of a solution containing xanthine (5 mM) and EDTA (15 mM) and 60 $\mu$L of XO (2.1 milliunits/mL) from stocks were added consecutively. The mixture was incubated at 37 °C for 20 min with occasional vortexing and spun down by centrifugation at 11000 rpm for 5 min, and a clear supernatant solution was discarded. The incubation time of $\gamma$-$Fe_2O_3$ nanoparticles with the X/XO superoxide generating system was optimized by monitoring this rection with a UV−vis spectrometer as described above. Finally, $H_2O_2$ (60 $\mu$L, 0.036 $\mu$M) and DMPO (20 $\mu$L, 2.74 $\mu$M) were added to the nanoparticles, and the mixture was incubated again (37 °C, 40 min) with occasional vortexing and spun down by centrifugation at 11000 rpm for 5 min. A clear solution was transferred to a PTFE capillary for EPR measurements.

**(5) Hydroxyl Radical Scavenging with DMSO.** Eighty-four microliters of a solution containing DMSO (0.7 M), DMPO (32.6 mM), and $H_2O_2$ (0.43 mM) was added to either $Fe_3O_4$ (3.2 mg) or xanthine/xanthine oxidase-activated $\gamma$-$Fe_2O_3$ (3.08 mg) nanoparticles vide supra. The resulting mixtures were incubated at 37 °C for 40 min with occasional vortexing; the nanoparticles were spun down by centrifugation (3 min at 12000 rpm), and a clear solution was transferred to a PTFE capillary for EPR measurements.

**(6) Iron Ion Leaching Test.** $Fe_3O_4$ nanoparticles (3.4 mg) were placed in a conical vial, and 50 $\mu$L of a 50 mM phosphate buffer solution (pH 7.4) was added. The suspension was incubated at 37 °C for 1 h, and the nanoparticles were spun down by a 10 min centrifugation at 11000 rpm. The obtained clear solution was then transferred to another conical vial and incubated for 40 min at 37 °C with 20 $\mu$L of DMPO (21.23 mM) and 60 $\mu$L of $H_2O_2$ (0.28 mM). The resulting solution was transferred to a PTFE capillary for EPR measurements.

**(7) Thermogravimetric Analysis.** Coated nanoparticles (3.146 mg of oleate-coated NP and 18.676 mg of BSA-coated NP) were placed in an open platinum pan and heated from room temperature to 600 °C at a heating rate of 20 °C/min under a continuous purge of $N_2$ gas.

**Acknowledgment.** We acknowledge equal support from U.S. Department of Energy Contract DE-FG02-02ER15354 to A.I.S. and National Science Foundation (NSF) Grant MCB-0451510 to T.I.S. J.O.S.P. is thankful to the NSF Alliances for Graduate Education and Professoriate Grant 0450102 for support during the summer 2008 project.

**Supporting Information Available:** FT-IR spectra, TGA data, and additional EPR spectra. This material is available free of charge via the Internet at http://pubs.acs.org.

JA104683W

(61) Alaouie, A. M.; Smirnov, A. I. *J. Magn. Reson.* **2006**, *182*, 229–238.
(62) Smirnov, A. I.; Belford, R. L. *J. Magn. Reson., Ser. A* **1995**, *113*, 65–73.
(63) Smirnova, T. I.; Smirnov, A. I.; Clarkson, R. B.; Belford, R. L. *J. Phys. Chem.* **1995**, *99*, 9008–9016.
(64) Fridovich, I. Xanthine oxidase. In *Handbook of methods for oxygen radical research*; Greenwald, R. A., Ed.; CRC Press: Boca Raton, FL, 1985; pp 51−53.